Applied Energy 353 (2024) 122068

Contents lists available at ScienceDirect

Applied Energy

journal homepage: www.elsevier.com/locate/apenergy

The catalytic effect of iron oxide phases on the conversion of cellulose-derived chars in diluted O_2 and CO_2 ☆

Christin Pflieger [a], Till Eckhard [a], Jannik Böttger [a], Jonas Schulwitz [a], Tim Herrendorf [b], Stefan Schmidt [a], Soma Salamon [c], Joachim Landers [c], Heiko Wende [c], Wolfgang Kleist [b], Martin Muhler [a,*], Francesca Cerciello [a,*]

[a] *Lehrstuhl für Technische Chemie, Ruhr-Universität Bochum, Universitätsstr. 150, 44801 Bochum, Germany*
[b] *Department of Chemistry, RPTU Kaiserslautern-Landau, Erwin-Schrödinger-Str. 54, 67663 Kaiserslautern, Germany*
[c] *Faculty of Physics and Center for Nanointegration Duisburg-Essen (CENIDE), Universität Duisburg-Essen, Lotharstr. 1, 47057 Duisburg, Germany*

HIGHLIGHTS

- Catalytic effect of Fe on biomass-derived model char conversion in O_2- and CO_2.
- γ-Fe_2O_3 transformation to ε-Fe_2O_3 during char oxidation with high catalytic activity.
- Additional transformation to α-Fe_2O_3 during oxidation without catalytic activity.
- γ-Fe_2O_3 transformation to FeO and to γ-Fe during char gasification.
- Partially re-oxidation of γ-Fe in CO_2 resulting in Fe_3O_4 remaining in the ash.

ARTICLE INFO

Keywords:
Biomass-derived char
Char conversion
Fe minerals
Catalytic activity
Phase transformation

ABSTRACT

The conversion of biomass-derived char is substantially influenced by its metal content. One of the main catalytically active metallic elements in biomass is Fe, which occurs in various mineral forms. For the implementation of catalytic effects into char conversion models, investigations on the role of mineral type and loading are required. In this work, the catalytic effect of an Fe sulfate loading series on the oxidation and gasification of an inherently mineral-free cellulose-derived char was analysed. Characterisation focused on the Fe phases present in the char identifying the transformation from $FeSO_4$ to γ-Fe_2O_3 during doping, and further to ε-Fe_2O_3 and α-Fe_2O_3 upon char oxidation as well as to FeO and γ-Fe upon char gasification. Very high loading-dependent activities of ε-Fe_2O_3 and FeO were quantified by kinetic modelling. These iron oxides strongly catalyse char conversion, lowering the activation energy by up to 14% and 18%, respectively, relative to the mineral-free char.

1. Introduction

For the reduction of global greenhouse gas emissions, a special focus lies on the combustion of biomass-derived fuels [1]. In the combustion process, char conversion is the rate-determining step [2] and may occur as solely oxidation in air (O_2/N_2) or combined oxidation and gasification in oxyfuel (O_2/CO_2) atmosphere [3,4]. Irrespective of the gaseous composition, char conversion may be strongly influenced by the mineral content of the biomass [5]. Current char conversion models do not account for mineral effects and need to be extended for an accurate prediction of the process [6]. Hence, the assessment of catalytic effects specific to different types and amounts of minerals typically contained in natural biomass is required.

Biomass contains different inorganic elements classified into micronutrients (concentrations ≤0.1%, dry basis) such as Cl, Cu, Mn, Ni, Mo, Zn, Fe, and macronutrients (concentrations ≥0.1%, dry basis) such as Mg, P, S, K, Mg, and Ca. Alkali metals and alkaline earth metals (AAEM) are the most abundant inorganic components in biomass [7]. Indeed,

---

☆ The short version of the paper was presented at ICAE2022, Bochum, Germany, Aug 8–11, 2022. This paper is a substantial extension of the short version of the conference paper.

* Corresponding authors.
E-mail addresses: muhler@techem.rub.de (M. Muhler), francesca.cerciello@rub.de (F. Cerciello).

https://doi.org/10.1016/j.apenergy.2023.122068
Received 26 May 2023; Received in revised form 18 September 2023; Accepted 30 September 2023

catalytic effects of AAEM on biomass thermochemical conversion processes to produce high-quality end-products (biochar, bio-oil, and biogas) in large-scale have been extensive revised [8].

Furthermore, the role of mineral matter (including Fe) as a catalyst for chemical and structural transformations during heat treatments in inert and CO_2 atmospheres was previously investigated. Pyrolysis was performed with a heated strip reactor (HSR) up to 1800 °C using both N_2 and CO_2 atmospheres on a mineral-free cellulose-derived char. The question was discussed whether Fe loading affects char reactivity through catalytic action or through changes in the carbonaceous structure. On the one side, iron minerals enhanced the reactivity exerting a positive catalytic effect on pyrolysis, gasification, and combustion reaction. On the other side, these minerals increased the graphitisation and structural ordering [9].

The same carbon model material doped with Fe, K, Na, Mg, and Ca sulfates was used to assess the relevance of catalytic activity in flat-flame burner (FBB) experiments with high heating rates typical of industrial oxy-fuel combustion systems. In particular, samples doped with Fe exhibited lower thermal stability and higher particle combustion temperatures in the FFB compared with the undoped model fuel [10].

Consequently, Fe is one of the major catalytically active metallic elements contained in biomass exhibiting significant effects on biomass conversion despite being typically present in lower amounts than AAEM. Different minerals containing Fe were found in biomass, and phase transformations were reported to occur during the combustion process [11]. For example, sulfates as primary Fe minerals can undergo dehydration and decomposition, resulting in different other sulfates, carbonates, or oxides depending on the atmosphere [12,13]. Typically, oxidative treatments finally result in differently stable Fe oxides. For these species of the general composition Fe_xO_y, not only different Fe oxidation states, but also different polymorphs of the same oxidation state need to be considered. Most prominently, Fe_2O_3 was found to undergo purely structural phase transformations upon particle agglomeration, from metastable γ-Fe_2O_3 over ε-Fe_2O_3 to the highly stable α-Fe_2O_3 [14]. Contrarily, char gasification may even lead to locally reducing conditions so that elemental Fe^0 and iron carbides are additional species possibly present during char conversion [15–17].

An exact determination of the mineral present during the conversion process is of high importance as the effect of minerals on char conversion was revealed to depend not only on the type of metal but also on the counterion [18]. This counterion dependence also provides an explanation of the different strength of catalytic effect of Fe minerals reported in literature.

Impregnating 4 wt% of Fe as $Fe(NO_3)_3$ on fir powder has been reported to reduce the activation energy of CO_2 gasification relative to the raw fir by only 4%, thereby having much less effect than the comparatively studied acetates of K, Na, and Ca [19]. However, 3 wt% of Fe impregnated as $Fe(NO_3)_2$ were found to strongly activate pistachio nut shell gasification, with a reactivity increase close to $NaNO_3$ and $Ca(NO_3)_2$ as the most active dopants [20]. Similarly, the effect of 20 wt% Fe_2O_3 on CO_2 gasification of a cellulose-based char was also pronounced, lowering the activation energy by about 17% [21]. With this activity higher than alkaline earth metal oxides but lower than alkali carbonates, Fe oxide exhibited an intermediate effect. A similarly strong catalytic effect can be assumed for $FeCl_3$ as the addition of 5 wt% to sugar cane bagasse was reported to lower the activation energy by around 11%.

Recent studies of Fe sulfate doping of a mineral-free model char even revealed a distinctly higher activity of this mineral compared with the analogous sulfates of alkali and alkaline earth metals [22]. As in situ X-ray diffraction (XRD) investigations of the pure salts have shown the Fe sulfate to be the only one prone to phase transformation upon heating in diluted O_2 or CO_2 [10], the presence of different Fe phases was discussed as the origin of the exceptional high activity. However, the occurrence of phase transformations may be influenced by interactions of the Fe mineral with the carbon matrix [23], so that a phase identification is required for the doped carbon materials and not just for the pure dopants.

In continuation of previous studies, this work focuses on the catalytic effect of Fe on char conversion. The inherently mineral-free model char was doped with a loading series of Fe sulfate and sample reactivity was investigated by temperature-programmed (TP) oxidation and gasification measurements in analogy to Ref. [22]. Changes in char reactivity were related not only to the amount but also to the type of Fe mineral phase present in the material as determined by a comprehensive characterisation based on Mössbauer spectroscopy, XRD, differential scanning calorimetry (DSC), and X-ray absorption spectroscopy (XAS). In combination with an extended kinetic modelling, mineral effects were assessed both qualitatively and quantitatively, finally enabling the establishment of detailed structure-activity correlations.

2. Materials and methods

2.1. Synthesis of the Fe-doped model fuel

In a first step, a mineral-free model char was synthesised by hydrothermal carbonisation of microcrystalline cellulose at 200 °C for 24 h and subsequent low heating rate pyrolysis at 800 °C for 2 h [21]. The hydrothermal carbonisation treatment was used to obtain a mineral-free reference sample. Subsequently, the pyrolysis step at 800 °C was performed to separate the contribution of devolatilisation from the oxidation/gasification step. The obtained MH800 char was then selectively doped with $FeSO_4{\bullet}7\ H_2O$ (supplied by VWR Chemicals) by wet impregnation [10], thereby loading 0.15–2.4 wt%. The synthesis was finished by drying at 105 °C in air, and the samples were labelled using their loading *w* as '*w* Fe-MH800'. For example, the sample loaded with 0.15 wt% Fe was labelled as '0.15 Fe-MH800'.

2.2. Temperature-programmed measurements

TP measurements were performed by heating about 30 mg of sample using a magnetic suspension balance [10]. For oxidation, heating was performed with 5 °C min^{-1} in 100 ml min^{-1} 20% O_2/He, while for gasification a heating rate of 1 °C min^{-1} was adjusted to finalise conversion in 100 ml min^{-1} 50% CO_2/He prior to the maximum temperature of 1100 °C. Measurement analysis relied on the differential thermogravimetric (DTG) curve, which was calculated as the normalised first derivative of the thermogravimetric mass loss curve:

$$\mathrm{DTG} = \frac{-\left(\frac{dm}{dT}\right)}{m_0 - m_f} \tag{1}$$

The change of mass m as a function of temperature T was related to the total converted mass, obtained as the difference of initial (m_0)and final sample mass (m_f).

2.3. Conversion modelling

For a quantification of the catalytic effect, the DTG curves as a measure of the change in conversion X were fitted using the random pore model (RPM) in its temperature-dependent form [24,25]:

$$\frac{dX}{dT} = \beta \bullet k_0 \bullet \left(\frac{-E_A}{RT}\right) \bullet (1-X)\sqrt{1-\Psi \bullet ln(1-X)} \bullet y^b \tag{2}$$

This reaction rate description is composed of different parts: The heating rate β, an Arrhenius term comprising the pre-exponential factor k_0, the activation energy E_A, and the gas constant R as well as a conversion- and pore-dependent term with the structural parameter Ψ and the influence of reactive gas mole fraction y to a certain reaction order b. For simplification and to reduce uncertainties, the pre-exponential factor and the gas-related reaction order were assumed to be independent of the loading and were hence taken as fixed values derived from previous isothermal measurements of the undoped char [21]:

$$k_{0,O_2} = 9 \times 10^8 \ (min - 1)$$

$$k_{0,CO_2} = 9 \times 10^7 (min - 1)$$

$$b_{O_2} = 1.14$$

$$b_{CO_2} = 0.51$$

2.4. Mineral characterisations

Mössbauer spectroscopy was performed in transmission geometry using a ^{57}Co(Rh) radiation source mounted on a driving unit operating in constant acceleration mode. The isomer shifts of spectra derived from about 210–230 mg of sample material were referenced against α-Fe at room temperature.

Powder X-ray diffraction (XRD) patterns were recorded using a diffractometer (Bruker Discover D8) equipped with θ - θ geometry, Lynxeye-1D detector, and Cu Kα radiation (0.15406 nm, 40 kV, 40 mA). The recording was performed in a 2θ range from 5 to 80° with 0.02° s^{-1} and data were evaluated using the software DIFFRAC.SUITE EVA with access to the International Centre for Diffraction Data database. Particle diameters were analysed according to the Scherrer equation [26] and Rietveld refinement was performed using the interface Profex 5.0.0 [27] with the backend BGMN [28]. The implemented database was extended using structural information from'The Materials Project' [29].

DSC measurements were performed in a Tian-Calvet type calorimeter implemented into a flow setup with effluent gas analysis as previously described [30]. 60 mg of sample were heated in 50 ml min^{-1} He from 30 °C to 800 °C with a heating rate of 5 °C min^{-1}. The also rate-controlled cooling was then followed by an isothermal period of 1 h at 50 °C in 50 ml min^{-1} 20% O_2/He, before heating up again.

XAS experiments were performed at the PETRA III Extension beamline P65 at Deutsches Elektronen-Synchrotron in Hamburg, Germany, with an energy range of 4–44 keV [31]. Measurements were performed at the Fe K-edge (7112 eV) using a Si(311) C-type double crystal monochromator and a beam current of 100 mA with a ring energy of 6.08 GeV. The samples were placed in glass capillaries without dilution and spectra were recorded as continuous scans in both fluorescence and transmission modes at ambient temperature and pressure in the range of −150–1000 eV around the edge in 180 s. Evaluation was performed using the Demeter software package on the fluorescence data of the individual samples as well as the selected Fe mineral samples Fe_3O_4, α-Fe_2O_3, γ-Fe_2O_3, and ε-Fe_2O_3 (phase pure according to XRD).

Raman measurements were performed using a spectrometer (LabRAM HR Evolution by Horiba Scientific) equipped with a green laser of 532 nm wavelength (by Oxxius). 0.1% of the total laser power of 100 mW in combination with a grating of 600 (500 nm) were used to measure the samples placed as powders on a microscopic slide with an integration over 900 s.

3. Results and discussion

3.1. TP measurement analysis

The DTG curves derived from the TP measurements of the Fe loading series are shown in Fig. 1 for oxidation as well as for gasification.

The analysis reveals a strong temperature shift of the peak maxima with increasing loading in both atmospheres and hence a loading-dependent catalytic effect. Starting with the analysis of char oxidation (Fig. 1a), the temperature of maximum oxidation rate is lowered by up to 129 °C compared with the undoped MH800. In addition to this remarkable shift in peak temperatures, a slightly altered peak shape was found for Fe-doped oxidation. In the high-temperature region of the conversion peaks between 550 and 600 °C an additional shoulder was observed especially for the higher loadings of Fe (red dashed line in Fig. 1a). The overall shape points towards catalytic char oxidation related to the main low-temperature peak and non-catalytic char oxidation related to the high-temperature shoulder as there is no significant temperature shift relative to the undoped char for this part.

There are two possible explanations for the observed non-catalytic char oxidation between 550 and 600 °C. On the one hand, it may be possible that the loading of Fe is too low to affect the entire carbon material, so that there are carbon sites without contact to Fe, which are therefore converted according to the non-catalytic pathway. On the other hand, there may be two different Fe mineral phases present during conversion, either simultaneously as a mixture or by transformation due to the temperature increase. Consequently, the (initially) active phase would cause the catalytic oxidation of char, whereas final conversion proceeds non-catalytically as there is only a comparatively inactive Fe

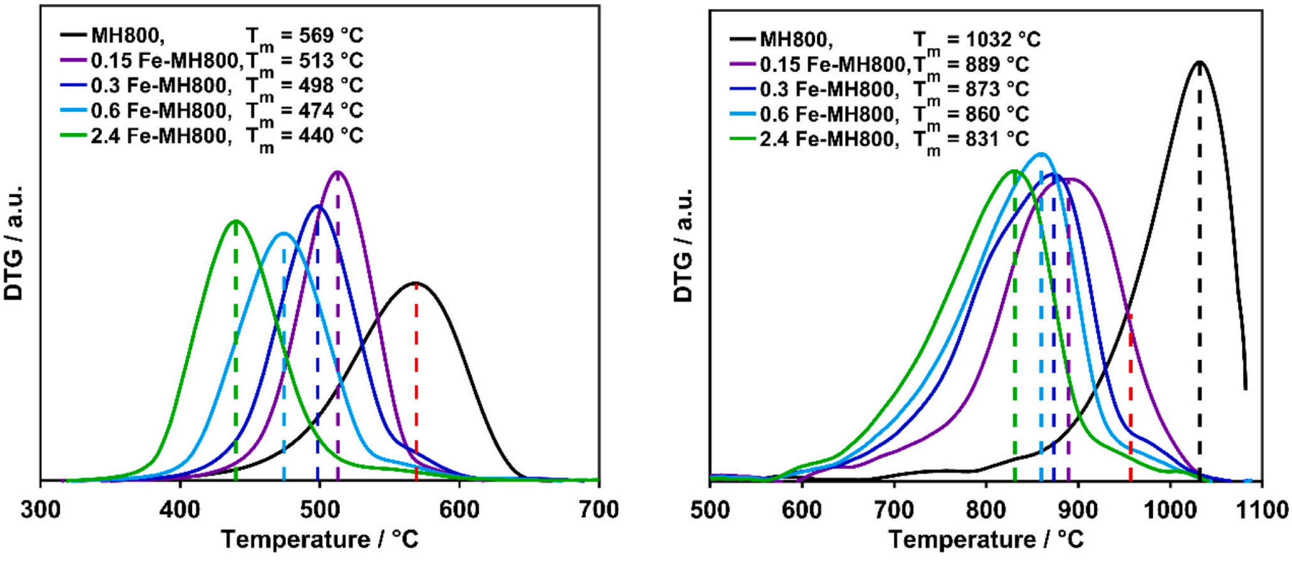

(a) Oxidation

(b) Gasification

Fig. 1. DTG curves of the Fe loading series with marked peak maxima.

phase present on the char, which may have been present from the beginning or resulted from phase transformation. In case of the first alternative of a too low Fe loading, a decreasing contribution of non-catalytic conversion would be expected for higher Fe loadings, as an increased occurrence of Fe would minimise the possibility of carbon sites being unaffected by Fe. As no such correlation is shown in the curves, the presence of two distinguishable contributions to conversion is assumed to originate from two different mineral phases of different catalytic activity.

The same behaviour is observed in the gasification curves (Fig. 1b). In addition to the peak maximum which is lowered by up to 201 °C relative to the undoped MH800, there is an intermediate shoulder lowered by around 70 °C (red dashed line in Fig. 1b). These positions indicate the presence of a highly active Fe phase below 900 °C and a less but still significantly active phase towards higher temperatures. A third contribution below 650 °C may be possible, as an additional shoulder is observed. However, the subsequent analysis focuses on the two more strongly contributing parts of the main peak and high temperature shoulder for both atmospheres. Therefore, the kinetic modelling of the DTG curves was performed using the sum of two RPM equations accounting for two individual contributions to overall conversion. In this way, the catalytic effects of the corresponding individual phases were quantified by the derived activation energy, i.e. by the activation energy decrease ΔE_A relative to the undoped MH800 ($E_{A,O_2} = 146$ kJ mol^{-1}, $E_{A,CO_2} = 239$ kJ mol^{-1}). For the mainly present Fe phase, a loading-dependent decrease of up to 20 kJ mol^{-1} (14%) for oxidation and up to 42 kJ mol^{-1} (18%) for gasification as shown in Fig. 2 was found.

In contrast, for the additional Fe phases leading to the shoulders in the conversion curves almost no activity ($\Delta E_A = 2$ kJ mol^{-1}) resulted in case of oxidation, but a slight activity ($\Delta E_A = 17$ kJ mol^{-1}) in case of gasification.

3.2. Fe phase analysis

For an assignment of specific Fe phases to the contributions identified in the DTG curves, the Fe-loaded chars were characterised at different points in sample history. The influence of conversion temperature and atmosphere was taken into account in the selection of representative samples for analysis by different characterisation methods with the potential to overcome limitations due to low mineral amounts in a dominating carbon matrix.

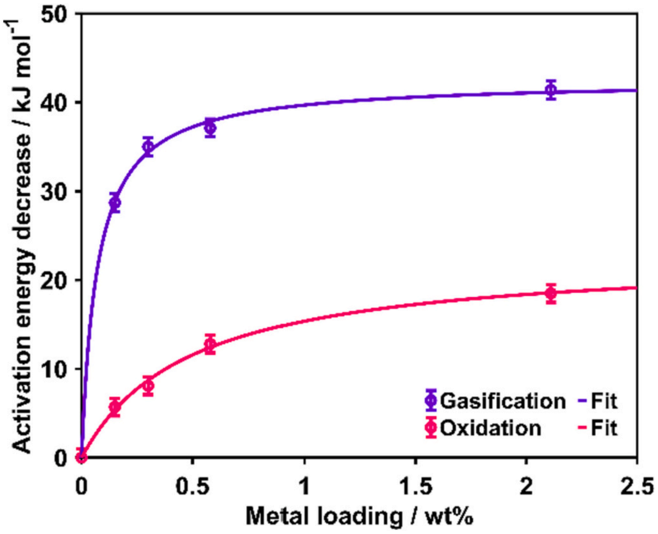

Fig. 2. Loading-dependent activation energy decrease relative to the undoped MH800.

3.2.1. As-synthesised char

The phase analysis of the as-synthesised char was performed using 2.4 Fe-MH800, as this highest loading was the most promising to achieve phase identification despite the dominating char material. The Mössbauer spectrum recorded for this sample at room temperature is presented in Fig. 3, showing a doublet with an isomer shift of 0.40 mm/s and a quadrupole splitting of ca. 0.72 mm/s, being characteristic for Fe^{3+} [32].

Consequently, the synthesis procedure led to an oxidised Fe mineral despite the doping with $FeSO_4$. Thereby, the carbon material would have significantly lowered the decomposition temperature of $FeSO_4$, as heating of the doped sample during drying was only performed up to a maximum temperature of 105 °C, which is well below the decomposition temperature of pure $FeSO_4$ (> 500 °C) [13]. A similar decrease of the $FeSO_4$ decomposition temperature due to a surrounding organic matrix has already been observed for lignite and bamboo, but to a lower extent than for the char material in this work [33,34].

For further analysis of the oxidised phase, XRD measurements were performed. While for the as-synthesised 2.4 Fe-MH800 the particles were too small to obtain mineral-related reflections and the broad carbon signals were dominating, the XRD pattern of the same sample obtained after isothermal treatment at 480 °C for 3 h in He (Fig. 4) was indicative of either γ-Fe_2O_3 or Fe_3O_4 particles. These phases are essentially undistinguishable by XRD as both oxide species crystallise in the same space group and feature similar lattice parameters [35].

However, in combination with the Mössbauer results revealing Fe^{3+}, γ-Fe_2O_3 is indicated to be the phase present after the synthesis procedure, presumably displaying a doublet structure due to superparamagnetic relaxation. Possible intermediates of the reaction from $FeSO_4 \bullet 7\ H_2O$ to iron oxide like $Fe(OH)SO_4$ or $Fe_2O(SO_4)_2$ can be clearly differentiated based on the observed spectrum. Although they also contain Fe^{3+}, showing an isomer shift comparable to our sample, they exhibit widely different values of quadrupole splitting [36–38].

Further, an evaluation of the XRD pattern of the heat-treated char revealed an iron oxide particle diameter of 12 nm. A comparison to the pattern of the as-synthesised char shows that a significant increase in particle size was induced by the thermal treatment at 480 °C, resulting in an increased mineral crystallinity and hence pronounced reflections. Considering this substantial thermally induced sintering [39], the particle diameter of γ-Fe_2O_3 after synthesis is known to be far below 12 nm.

3.2.2. Thermal degradation

To distinguish the effects of atmosphere and temperature, an analysis of the phase transformations upon inert heating was performed by DSC. In this way, it is possible to obtain the exact temperature range, while concurrently recording the enthalpy difference of involved phases and

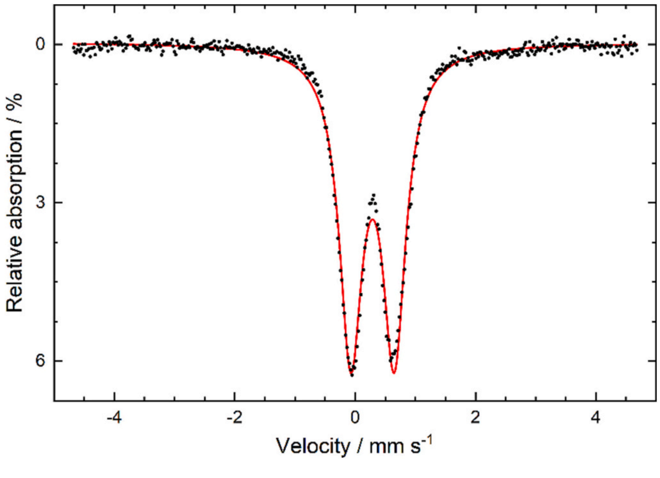

Fig. 3. Mössbauer spectrum of 2.4 Fe-MH800 recorded at room temperature.

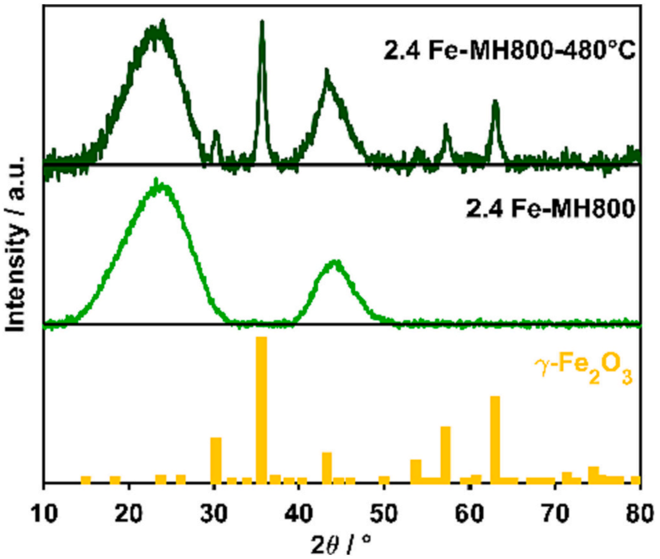

Fig. 4. XRD patterns of 2.4 Fe-MH800 as-synthesised and after 3 h of isothermal treatment in He.

possibly evolving gases. Fig. 5 shows the heat flow and the evolving gases during the inert heating of 2.4 Fe-MH800 as-synthesised and in O_2 at 50 °C for 1 h. During the first heating of 2.4 Fe-MH800, a heat effect by phase transformation was only observed at a temperature of about 700 °C, associated with a pronounced release of CO.

After isothermal treatment in O_2 at 50 °C, the sequential second heating in the DSC led to equal amounts of consumed heat and evolved CO as during the first heating, however at slightly higher temperatures of 730 °C. Consequently, full phase reversibility was demonstrated, along with the potential sintering of particles leading to the observed temperature shift and peak narrowing. For phase identification, a correlative quantification of heat flow and CO evolution was performed. The following amounts related to the molar amount of Fe were derived by peak integration:

$$Q_m = 75 \text{ kJ mol}^{-1}(\text{Fe}).$$

$$n_{CO} = 0.47 \text{ mol mol}^{-1}(\text{Fe}).$$

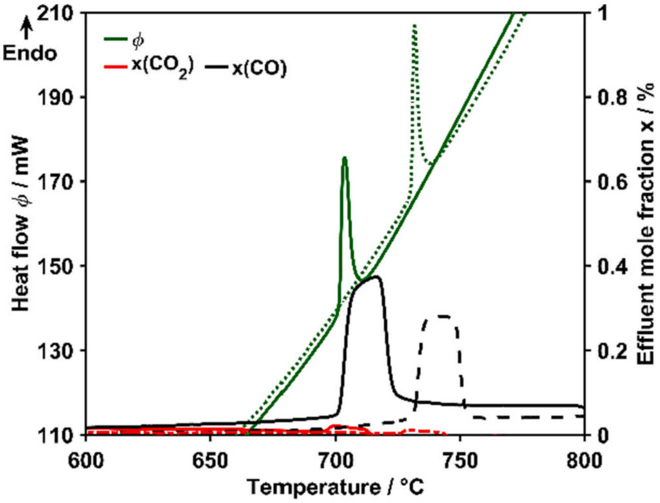

Fig. 5. Heat flow and effluent gas curves during the inert heating of 2.4 Fe-MH800 as-synthesised (solid line) in 50 ml min^{-1} He, and during a second inert heating after an intermediate isothermal treatment in O_2 at 50 °C (dashed line).

The absence of any reactive gas limits the possible origins of the endothermic effect and CO release to an interaction of the char and the γ-Fe_2O_3 particles. With Fe being already in its highest oxidation state, the oxidation of γ-Fe_2O_3 by CO_2 abstracted from the char does not serve as a possible explanation. Conversely, a reduction of the Fe phase is possible and may explain the observed effects in combination with a concurrent gasification of char according to one or even several of the following coupled reactions, referred to the molar amount of Fe [40–42]:

$$\frac{1}{2}\ Fe_2O_3 + \frac{1}{6}\ CO \rightleftharpoons \frac{1}{3}\ Fe_3O_4 + \frac{1}{6}\ CO_2 \tag{3}$$

$$\frac{1}{6}\ C + \frac{1}{6}\ CO_2 \rightleftharpoons \frac{1}{3}\ CO \tag{4}$$

$$\frac{1}{3}\ Fe_3O_4 + \frac{1}{3}\ CO \rightleftharpoons FeO + \frac{1}{3}\ CO_2 \tag{5}$$

$$\frac{1}{3}\ c + \frac{1}{3}\ CO_2 \rightleftharpoons \frac{2}{3}\ co \tag{6}$$

$$FeO + CO \rightleftharpoons Fe + CO_2 \tag{7}$$

$$C + CO_2 \rightleftharpoons 2\ CO \tag{8}$$

In these reactions, the initial CO is randomly abstracted from the char material (e.g. due to the decomposition of oxygen-containing functional groups) and initiates a self-promoting heterogeneous reaction sequence [43].

The heat effects associated to these equations are summarised in Table 1, assuming the γ-polymorph of Fe_2O_3.

As both conditions of heat effect and evolved CO need to be fulfilled, the most likely combination of the above reactions is the reduction of γ-Fe_2O_3 to FeO [46,47], which may occur via an intermediate Fe_3O_4 phase, and the consecutive gasification of char with an Fe/C stoichiometry of 2:1 and an endothermic heat effect of 76 kJ mol^{-1}. Thus, it can be concluded that the γ-Fe_2O_3 phase present at temperatures of up to 675 °C in the char matrix is then transformed into FeO, which is stable in inert atmosphere up to at least 800 °C, but being retransformed by exposure to O_2 after cooling [48]. The identified phase transformation also fits well to the observed sintering effect, as iron oxide particles were reported to be prone to sintering upon formation of FeO as an intermediate due to reduction [49].

3.2.3. *Transformation by oxidation*

In contrast to thermal degradation, a study of phase transformations during heating in an oxidative atmosphere was not possible by DSC due to the dominating exothermicity of carbon oxidation. Hence, the transformation by oxidation was investigated by analysis of samples collected after selective treatments. As no significant oxidation was observed up to 300 °C in the TP experiments, samples isothermally treated at this temperature were taken to represent the Fe phase prior to char conversion, whereas the ash of samples converted at 480 °C was analysed representative for the Fe phase after char conversion. Due to the unaffected amount of char after the treatment at 300 °C, XAS was used for phase characterisation. The linear combination fit of the obtained curves resulted in the phase distribution as shown in Fig. 6 [50]. In contrast to the inert treatment and despite the lower temperature of

Table 1
Heat effects calculated from standard formation enthalpies for the possible reactions of combined Fe reduction and char (C) gasification [44,45].

Eq.	ΔH (Fe)	ΔH (C)	ΔH (Fe + C)
(3) + (4)	−17	29	12
(5) + (6)	7	57	64
(7) + (8)	11	172	183

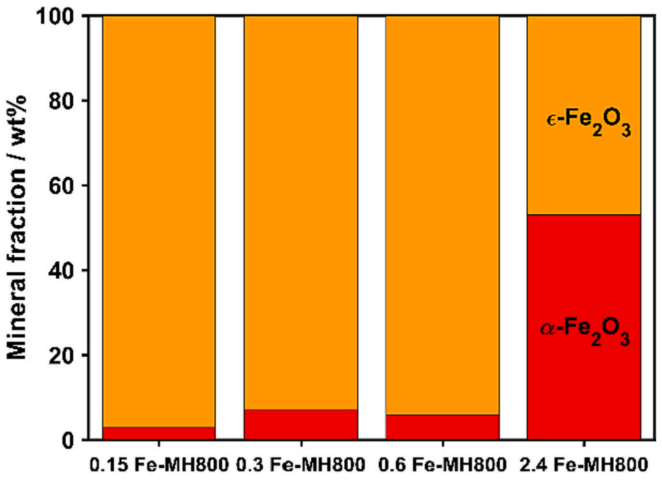

Fig. 6. Mineral phase distributions of the differently loaded chars after an oxidative treatment for 3 h at 300 °C determined by a linear combination fit of XAS results [51].

treatment, the oxidising atmosphere seems to have affected the Fe phase more strongly resulting in a complete transformation of γ-Fe_2O_3 to other polymorphs, mainly ε-Fe_2O_3 with a slight contribution of α-Fe_2O_3 for the lower loadings and an about equimolar combination of these for the highest loading.

In addition to the mild oxidation, a more severe oxidising treatment at 480 °C was applied, resulting in a complete conversion of the carbon material. For the corresponding ash samples, XRD (Fig. 7) revealed that ε-Fe_2O_3 and α-Fe_2O_3 remained after oxidation.

Therefore, these two phases are assumed to be decisive for char oxidation with a clear loading dependence of their relative abundance and relevance. For further analysis, a quantification of the individual phase contributions by a Rietveld refinement of the XRD patterns of the ash samples was performed. The results are summarised in Table 2 along with the particle diameters.

The loading dependence of both phase composition and particle size is clearly demonstrated. While for the lowest loading ε-Fe_2O_3 remained predominant during the more severe oxidation and the concurrent loss of the carbon matrix, oxidation of the intermediate loadings was associated with further significant transformation to α-Fe_2O_3. For the highest loading, α-Fe_2O_3 even became the main fraction present after oxidation. Simultaneously, the particles of both phases were found to increase in size with increasing loading. The particle diameter of the minerals during the phase transformation from ε-Fe_2O_3 to α-Fe_2O_3 is found to be in the range of 17–19 nm. However, for the previous transformation of γ-Fe_2O_3 to ε-Fe_2O_3 no size range can be stated as for both phases particles of 12 nm diameter were found. Therefore, this structural transformation is indicated to be induced by exposing the material to an oxidative atmosphere.

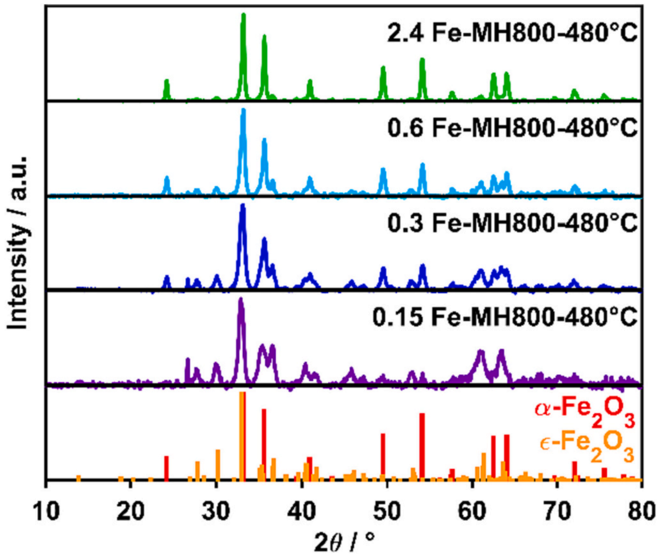

Fig. 7. XRD patterns of differently loaded Fe-MH800 samples after isothermal conversion for 3 h in 20% O_2/He.

Table 2
Phase contributions c and particle diameters d_P of the ash samples remaining after oxidation of differently loaded Fe-MH800 for 3 h at 480 °C.

Loading	α-Fe_2O_3		ε-Fe_2O_3	
/ wt%	c / -	d_P / *nm*	c / -	d_P / *nm*
0.15	0.03	*n.d.*	0.97	12
0.3	0.20	19	0.80	12
0.6	0.30	25	0.70	15
2.4	0.62	31	0.38	17

n.d. not detectable due to the low amount of α-Fe_2O_3.

Combining the phase analysis with the TP measurement results, the mainly present Fe mineral during oxidation is the highly active ε-Fe_2O_3 forming small particles, while increased loadings and progressing char conversion enhance particle agglomeration and hence the transformation to the larger α-Fe_2O_3 particles, contributing to a much lower extent to catalytic char oxidation.

3.2.4. *Transformation by gasification*

The TP gasification measurements indicated the presence of three different phases with transformations possibly occurring around 650 °C and 950 °C. Remarkably, the first temperature range shortly after the onset of gasification is also the temperature range of phase transformation determined for the solely thermal treatment. Hence, a phase similarity in inert and gasifying atmosphere can be assumed. As the phase transformation during inert heating was found to be initiated by CO, the larger concentrations due to already ongoing gasification may have shifted the phase transformation to slightly lower temperatures in CO_2. Additionally, the initiation of carbon conversion prior to the range of phase transformation is likely to hamper the autocatalytic process observed in inert atmosphere, and hence a broadening of the transformation range may occur. Consequently, the main catalytically active phase for gasification at 650–900 °C is derived to be FeO [16,52]. In the previous DSC experiment (Fig. 5), the reversibility of the phase transformation after heating to maximum 800 °C was observed, so that an analysis of partially gasified samples is not meaningful.

During the TP experiments, heating in the gasification atmosphere was performed up to 1100 °C, during which another phase was indicated to dominate the catalytic conversion about 900 °C. Due to still progressing gasification, a rather large CO concentration on the char surface is expected for this temperature range, so that further reduction of the mineral phase is likely. This is in good agreement with literature observing the transformation of FeO to γ-Fe at temperatures of about 900 °C [16,42,53]. Hence, a characterisation of the mineral phase resulting from gasification was performed by retrieving the ash after a TP experiment. Without remaining carbon, a phase identification by Raman spectroscopy was possible (Fig. 8).

Although Fe_3O_4 was clearly detected, there is no contradiction to the assumed presence of γ-Fe at high gasification temperatures. The elemental form is only stable in a reducing environment, but during the TP experiment the sample was still heated in CO_2 when the char was already consumed, and therefore no further CO release by gasification occurred. Similar to the reverse transformation of the mid-temperature FeO phase, the exposure of γ-Fe to CO_2 at high temperatures seems to have resulted in a re-oxidation forming Fe_3O_4 [18,55], which is known to be stable in CO_2 atmosphere [17,49,56].

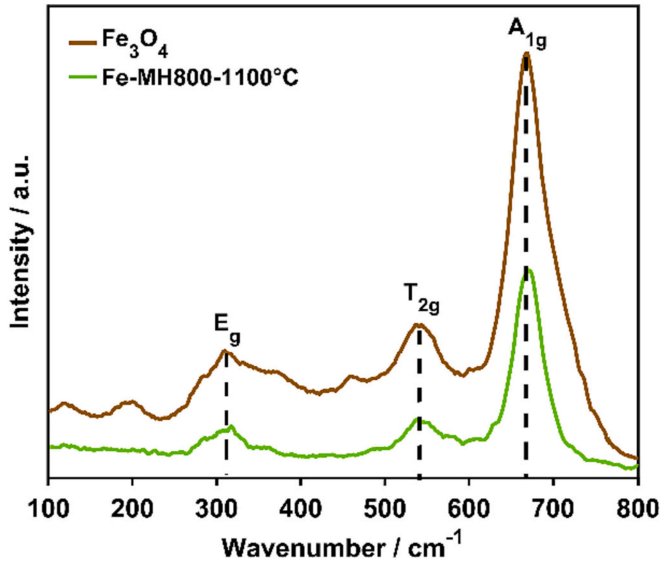

Fig. 8. Raman spectra of the ash remaining after TP gasification of Fe-doped samples up to 1100 °C and of an Fe_3O_4 reference with the symmetry assignment [54] marked by dashed lines.

3.2.5. *Oxidation vs. gasification phase transformations*

Combining the phase analysis with the TP measurement results, differently active contributions to char conversion were observed due to the presence of different Fe mineral phases.

Drying the sample at 105 °C in air after the doping procedure described in Section 2.1, was sufficient to oxidise the $FeSO_4$ as impregnated on the char to the metastable γ-Fe_2O_3. γ-Fe_2O_3 (mineralogically known as maghemite) is the second most common Fe_2O_3 polymorph in nature. It exists in both bulk and nanosized forms. γ-Fe_2O_3 has a cubic crystal structure of an inverse spinel type and crystallises in the *P4₁32* space group. γ-Fe_2O_3 as a typical ferrimagnetic material is thermodynamically unstable. It is converted either directly or indirectly (with ε-Fe_2O_3 as an intermediate product) to α-Fe_2O_3 when the temperature exceeds a threshold value.

During oxidation up to 300 °C, prior to significant char conversion, transformation of γ-Fe_2O_3 to ε-Fe_2O_3 took place. ε-Fe_2O_3 was the main phase present during char oxidation lowering the activation energy by up to $\Delta E_A = 20$ kJ mol^{-1} (14%). With increasing Fe loading and carbon conversion, an additional transformation to α-Fe_2O_3 occurred. However, α-Fe_2O_3 exhibited no significant catalytic activity and a negligible contribution to catalytic char oxidation. α-Fe_2O_3 (mineralogically known as hematite) has a rhombohedrally centered hexagonal structure of the corundum type with a close-packed oxygen lattice in which two-thirds of the octahedral sites are occupied by Fe(III) ions. It crystallises in the $R\overline{3}c$ space group. Above 685 °C, α-Fe_2O_3 loses its magnetic ordering and becomes paramagnetic. α-Fe_2O_3 is one of the final products of thermal decomposition of a variety of Fe(II)- and Fe(III)-containing compounds and, therefore, it is more easy to be synthesised. ε-Fe_2O_3 is a rare polymorph that exists only in the form of nanostructures. It has an orthorhombic crystal structure with the *Pna21* space group. Around 220 °C, ε-Fe_2O_3 changes from a paramagnetic to a magnetic state [57]. During the oxidation tests, it is possible that the porous carbon matrix of the char sample acted as an anti-sintering agent, prolonging the lifetime of the metastable ε-Fe_2O_3 and preventing its transformation to α-Fe_2O_3 even at 480 °C.

During gasification around 700 °C, CO released by carbon conversion induced phase transformations from γ-Fe_2O_3 to FeO. The latter was the main active phase lowering the activation energy up to $\Delta E_A = 42$ kJ mol^{-1} (18%). Further heating to about 900 °C induced another transformation to the less active γ-Fe (lowering of activation energy up to $\Delta E_A = 17$ kJ mol^{-1}). During char gasification, iron reduction occurred combined with char gasification as a self-promoting reaction. Upon complete char consumption, the Fe mineral was partly re-oxidised by CO_2, resulting in Fe_3O_4 remaining in the ash. The Fe ions of Fe_3O_4 have a mixed valence state (2+/3+), which allows this material to catalyse both oxidation/reduction and acid/base reactions [58].

Besides the catalytical influence of iron oxides during biomass conversion, tar cracking, water-gas shift reaction, and forward Boudouard reactions are also promoted by iron-based catalysts. Therefore, the need for an abundant, cost-effective, and preferably non-toxic catalyst is still a significant area of interest for gasification technology. The presence of various compounds (reducing and oxidising agents) generated in a gasification reactor influences the nature and the performance of the catalyst, underlining the general importance of redox behaviour studies in the presence of carbon materials [59].

4. Conclusions

A mineral-free model char obtained by hydrothermal treatment of cellulose was first completely pyrolysed at 800 °C and then doped with a loading series of Fe sulfate. The sample reactivity was investigated by TP oxidation and gasification measurements. Changes in char reactivity were related to the amount and to the type of Fe mineral phase present in the material determined by Mössbauer spectroscopy, XRD, DSC, and XAS.

Combining the phase analysis with the TP measurement results, differently active contributions to char conversion were observed due to the presence of different Fe mineral phases.

Both TP oxidation and gasification measurements revealed a strong temperature shift of the peak maxima with increasing loading and hence a loading-dependent catalytic effect on char conversion. However, in the high-temperature region of conversion, between 550 and 600 °C in oxidation and above 900 °C in gasification, additional shoulders were observed. Therefore, the kinetic modelling of the DTG curves was performed using the sum of two RPM equations accounting for two individual contributions to overall conversion. The catalytic effects of the corresponding individual phases were quantified by the derived activation energy.

During oxidation, the strong catalytic effect was ascribed to ε-Fe_2O_3 forming small particles, while the progressing char conversion enhanced the formation of larger α-Fe_2O_3 particles, resulting in a lower contribution to char oxidation generating the shoulder in the DTG plots.

In gasification, the reduction of γ-Fe_2O_3 to FeO occurred combined with char gasification as a self-promoting reaction. FeO was the main active phase with a loading-dependent activation energy, while around 900 °C further reduction to the less active γ-Fe took place generating the shoulder in the DTG plots. Moreover, upon complete char consumption, the Fe mineral was partly re-oxidised by CO_2, resulting in Fe_3O_4 remaining in the ash.

Overall, Fe minerals were found to be very prone to phase transformations, resulting in a variety of possibly occurring phases during conversion of biomass-derived chars which strongly alter the catalytic effect.

CRediT authorship contribution statement

Christin Pflieger: Writing – original draft, Methodology, Formal analysis, Data curation, Conceptualization. **Till Eckhard:** Writing – original draft, Formal analysis, Data curation. **Jannik Böttger:** Writing – original draft, Formal analysis, Data curation. **Jonas Schulwitz:** Writing – original draft, Formal analysis, Data curation. **Tim Herrendorf:** Writing – original draft, Formal analysis, Data curation. **Stefan Schmidt:** Writing – original draft, Data curation, Conceptualization. **Soma Salamon:** Writing – original draft, Formal analysis, Data curation. **Joachim Landers:** Writing – original draft, Formal analysis, Data curation. **Heiko Wende:** Writing – original draft, Formal analysis, Data curation. **Wolfgang Kleist:** Writing – original draft, Methodology, Data

curation. **Martin Muhler:** Writing – original draft, Supervision, Methodology, Formal analysis, Data curation, Conceptualization. **Francesca Cerciello:** Writing – original draft, Supervision, Data curation.

Declaration of Competing Interest

The authors declare the following financial interests/personal relationships which may be considered as potential competing interests:

Christin Pflieger reports financial support was provided by German Research Foundation. Till Eckhard reports financial support was provided by German Research Foundation. Jannik Boettger reports financial support was provided by German Research Foundation.

Data availability

Data will be made available on request.

Acknowledgement

Funded by the Deutsche Forschungsgemeinschaft (DFG, German Research Foundation) –Project-ID 215035359– CRC/TRR 129 Oxyflame."Gefördert durch die Deutsche Forschungsgemeinschaft (DFG) –Projektnummer 215035359– CRC/TRR 129 Oxyflame".

Funded by the Deutsche Forschungsgemeinschaft (DFG, German Research Foundation) – Project-ID 388390466– CRC/TRR 247."Gefördert durch die Deutsche Forschungsgemeinschaft (DFG) –Projektnummer 388390466– CRC/TRR 247".

We acknowledge DESY (Hamburg, Germany), a member of the Helmholtz Association HGF, for the provision of experimental facilities. Parts of this research were carried out at Petra III and we would like to thank Dr. Edmund Welter for assistance in using beamline P65 (proposal I-20200918).

References

[1] Roncancio R, Gore JP. CO2 char gasification: a systematic review from 2014 to 2020. Energy Convers Manag X 2021;10:100060.

[2] Du Y, Wang C, Xin H, Che D, Mathews JP. Atomistic simulation of coal char oxy-fuel combustion: quantifying the influences of CO 2 to char reactivity. Energy Fuel 2019;33(10):10228–36.

[3] Spiegl N, Long X, Berrueco C, Paterson N, Millan M. Oxy-fuel co-gasification of coal and biomass for negative CO2 emissions. Fuel 2021;306:121671.

[4] Donnison C, Holland RA, Hastings A, Armstrong L-M, Eigenbrod F, Taylor G. Bioenergy with carbon capture and storage (BECCS): finding the win–wins for energy, negative emissions and ecosystem services—size matters. GCB Bioenergy 2020;12(8):586–604.

[5] Duman G, Uddin MA, Yanik J. The effect of char properties on gasification reactivity. Fuel Process Technol 2014;118:75–81.

[6] Branca C, Di Blasi C. Burning dynamics of straw chars under the conditions of thermal analysis. Energy Fuel 2021;35(15):12187–99.

[7] de Jong W, van Ommen JR. Biomass as a sustainable energy source for the future: Fundamentals of conv. John Wiley & Sons; 2014.

[8] Ong HC, Chen W-H, Farooq A, Gan YY, Lee KT, Ashokkumar V. Catalytic thermochemical conversion of biomass for biofuel production: a comprehensive review. Renew Sustain Energy Rev 2019;113:109266.

[9] Apicella B, Russo C, Ciajolo A, Cortese L, Cerciello F, Stanzione F, et al. High temperature pyrolysis of lignite and synthetic carbons. Fuel 2019;241:264–72.

[10] Eckhard T, Pflieger C, Schmidt S, Böttger J, Senneca O, Schiemann M, et al. Catalytic effects for cellulose-based model fuels under low and high heating rate in air and oxy-fuel atmosphere. Fuel 2022;324:124437.

[11] Vassilev SV, Baxter D, Vassileva CG. An overview of the behaviour of biomass during combustion: part I. Phase-mineral transformations of organic and inorganic matter. Fuel 2013;112:391–449.

[12] Vassilev SV, Baxter D, Andersen LK, Vassileva CG. An overview of the composition and application of biomass ash. Fuel 2013;105:19–39.

[13] Masset P, Poinso JY, Poignet JC. TG/DTA/MS study of the thermal decomposition of FeSO4·6H2O. J Therm Anal Calorim 2006;83(2):457–62.

[14] Sakurai S, Namai A, Hashimoto K, Ohkoshi S-I. First observation of phase transformation of all four Fe(2)O(3) phases (gamma – epsilon – beta – alpha-phase). J Am Chem Soc 2009;131(51):18299–303.

[15] Chew LM, Kangvansura P, Ruland H, Schulte HJ, Somsen C, Xia W, et al. Effect of nitrogen doping on the reducibility, activity and selectivity of carbon nanotube-supported iron catalysts applied in CO2 hydrogenation. Appl Catal Gen 2014;482:163–70.

[16] Gomez-Martin A, Schnepp Z, Ramirez-Rico J. Structural evolution in Iron-catalyzed graphitization of hard carbons. Chem Mater 2021;33(9):3087–97.

[17] Huang Z, He F, Zhu H, Chen D, Zhao K, Wei G, et al. Thermodynamic analysis and thermogravimetric investigation on chemical looping gasification of biomass char under different atmospheres with Fe2O3 oxygen carrier. Appl Energy 2015;157:546–53.

[18] Zhou Z, Hu Q, Liu X, Yu G, Wang F. Effect of Iron species and calcium hydroxide on high-sulfur petroleum coke CO 2 gasification. Energy Fuel 2012;26(3):1489–95.

[19] Huang Y, Yin X, Wu C, Wang C, Xie J, Zhou Z, et al. Effects of metal catalysts on CO2 gasification reactivity of biomass char. Biotechnol Adv 2009;27(5):568–72.

[20] Lahijani P, Zainal ZA, Mohamed AR, Mohammadi M. CO2 gasification reactivity of biomass char: catalytic influence of alkali, alkaline earth and transition metal salts. Bioresour Technol 2013;144:288–95.

[21] Pflieger C, Lotz K, Hilse N, Berger CM, Schiemann M, Debiagi P, et al. Catalytic influence of mineral compounds on the reactivity of cellulose-derived char in O2-, CO2-, and H2O-containing atmospheres. Fuel 2021;287:119584.

[22] Eckhard T, Pflieger C, Böttger J, Telaar P, Cerciello F, Muhler M. The catalytic effect of iron, alkali and alkaline earth metal sulfates loading series on the conversion of cellulose-derived hydrochars and chars. ACS Omega 2023;8(11):10629–39.

[23] Lotz K, Wütscher A, Düdder H, Berger CM, Russo C, Mukherjee K, et al. Tuning the properties of iron-doped porous graphitic carbon synthesized by hydrothermal carbonization of cellulose and subsequent pyrolysis. ACS Omega 2019;4(2):4448–60.

[24] Adamon DGF, Fagbémi LA, Bensakhria A, Sanya EA. Comparison of kinetic models for carbon dioxide and steam gasification of Rice husk char. Waste Biomass Valor 2019;10(2):407–15.

[25] Zhang J-L, Wang G-W, Shao J-G, Zuo H-B. A modified random pore model for the kinetics of char gasification. BioResources 2014;9(2):3497–507.

[26] Ali K, Sarfraz AK, Mirza IM, Bahadur A, Iqbal S. Ul Haq a. preparation of superparamagnetic maghemite (γ-Fe2O3) nanoparticles by wet chemical route and investigation of their magnetic and dielectric properties. Curr Appl Phys 2015;15(8):925–9.

[27] Doebelin N, Kleeberg R. Profex: a graphical user interface for the Rietveld refinement program BGMN. J Appl Cryst 2015;48(Pt 5):1573–80.

[28] Bergmann Jörg, Friedel Peter, Kleeberg Reinhard. BGMN — a new fundamental parameters based Rietveld program for laboratory X-ray sources, it's use in quantitative analysis and structure investigations. CPD Newsletter; 2023.

[29] Jain A, Ong SP, Hautier G, Chen W, Richards WD, Dacek S, et al. Commentary: the materials project: a materials genome approach to accelerating materials innovation. APL Mater 2013;1(1):11002.

[30] Pflieger C, Eckhard T, Schmitz G, Angenent V, Göckeler M, Senneca O, et al. Thermicity of the decomposition of oxygen functional groups on cellulose-derived chars. ACS Omega 2022;7(51):48606–14.

[31] Welter E, Chernikov R, Herrmann M, Nemausat R. A beamline for bulk sample x-ray absorption spectroscopy at the high brilliance storage ring PETRA III. Author(s); 2019. p. 40002.

[32] Devi L, Craje M, Thüne P, Ptasinski KJ, Janssen FJ. Olivine as tar removal catalyst for biomass gasifiers: catalyst characterization. Appl Catal Gen 2005;294(1):68–79.

[33] Zhang D, Yani S. Sulphur transformation during pyrolysis of an Australian lignite. Proc Combust Inst 2011;33(2):1747–53.

[34] Pace B, Munroe P, Marjo CE, Thomas P, Gong B, Shepherd J, et al. The mechanisms and consequences of inorganic reactions during the production of ferrous sulphate enriched bamboo biochars. J Anal Appl Pyrolysis 2018;131:101–12.

[35] Katikaneani P, Vaddepally AK, Reddy Tippana N, Banavath R, Kommu S. Phase transformation of Iron oxide nanoparticles from hematite to Maghemite in presence of polyethylene glycol: application as corrosion resistant nanoparticle paints. J Nanosci 2016;2016:1–6.

[36] Petkova V, Pelovski Y. Investigation on the thermal properties of Fe2O(SO4)2. Part I J Therm Anal Calorim 2001;64(3):1025–35.

[37] Petkova V, Pelovski Y. Investigation on the thermal properties of Fe2O(SO4)2. Part II J Therm Anal Calorim 2001;64(3):1037–44.

[38] Skeff Neto K, Miranda L. Magnetic properties of FeOHSO4- I. Mössbauer Spectr Solid State Commun 1978;28(1):43–8.

[39] Kramer CM, German RM. Low-temperature sintering of Iron oxides. J Am Ceram Soc 2006;61(7–8):340–2.

[40] Liu G-S, Niksa S. Coal conversion submodels for design applications at elevated pressures. Part II. Char gasification. Prog Energy Combust Sci 2004;30(6):679–717.

[41] Iguchi Y, Endo S. Reactions, coalescence of reduced Iron particles, and liberation of carbon particles in carbon composite Iron ore pellets. ISIJ Int 2004;44(12):1999–2007.

[42] Neeli ST, Ramsurn H. Synthesis and formation mechanism of iron nanoparticles in graphitized carbon matrices using biochar from biomass model compounds as a support. Carbon 2018;134:480–90.

[43] Brown TA, Dennis JS, Scott SA, Davidson JF, Hayhurst AN. Gasification and chemical-looping combustion of a lignite char in a fluidized bed of Iron oxide. Energy Fuel 2010;24(5):3034–48.

[44] Chase M. NIST-JANAF thermochemical tables, 4th edition: American Institute of Physics, −1. 1998.

[45] Majzlan J, Navrotsky A, Schwertmann U. Thermodynamics of iron oxides: part III. Enthalpies of formation and stability of ferrihydrite (∼Fe(OH)3), schwertmannite (∼FeO(OH)3/4(SO4)1/8), and ε-Fe2O3. Geochim Cosmochim Acta 2004;68(5):1049–59.

[46] Hu Q, Yao D, Xie Y, Zhu Y, Yang H, Chen Y, et al. Study on intrinsic reaction behavior and kinetics during reduction of iron ore pellets by utilization of biochar. Energ Conver Manage 2018;158:1–8.

[47] Huang Z, Zhang Y, Fu J, Yu L, Chen M, Liu S, et al. Chemical looping gasification of biomass char using iron ore as an oxygen carrier. Int J Hydrogen Energy 2016;41 (40):17871–83.
[48] Wei G, Wang H, Zhao W, Huang Z, Yi Q, He F, et al. Synthesis gas production from chemical looping gasification of lignite by using hematite as oxygen carrier. Energ Conver Manage 2019;185:774–82.
[49] Hu J, Poelman H, Marin GB, Detavernier C, Kawi S, Galvita VV. FeO controls the sintering of iron-based oxygen carriers in chemical looping CO2 conversion. J CO2 Util 2020;40:101216.
[50] Alvarez J, Lopez G, Amutio M, Bilbao J, Olazar M. Evolution of biomass char features and their role in the reactivity during steam gasification in a conical spouted bed reactor. Energ Conver Manage 2019;181:214–22.
[51] López-Sánchez J, Serrano A, Del Campo A, Muñoz-Noval Á, Salas-Colera E, Cabero M, et al. A combined micro-Raman, X-ray absorption and magnetic study to follow the glycerol-assisted growth of epsilon-iron oxide sol-gel coatings. J Alloys Compd 2022;892:162061.
[52] Liu G-S, Strezov V, Lucas JA, Wibberley LJ. Thermal investigations of direct iron ore reduction with coal. Thermochim Acta 2004;410(1–2):133–40.
[53] Seaton CE, Foster JS, Velasco J. Structural changes occurring during reduction of hematite and magnetite pellets containing coal char. ISIJ Int 1983;23(6):497–503.
[54] Shebanova ON, Lazor P. Raman spectroscopic study of magnetite (FeFe2O4): a new assignment for the vibrational spectrum. J Solid State Chem 2003;174(2):424–30.
[55] Spreitzer D, Schenk J. Reduction of iron oxides with hydrogen—a review. Steel Res Int 2019;90(10):1900108.
[56] Yu D, Yu X, Wu J, Han J, Liu F, Pan H. A comprehensive review of ash issues in Oxyfuel combustion of coal and biomass: mineral matter transformation, ash formation, and deposition. Energy Fuel 2021;35(21):17241–60.
[57] Machala L, Tuček J, Zbořil R. Polymorphous transformations of Nanometric Iron (III) oxide: a review. Chem Mater 2011;23(14):3255–72.
[58] Cornell RM, Schwertmann U. The iron oxides. Wiley; 2003.
[59] Ramadhani B, Kivevele T, Kihedu JH, Jande YAC. Catalytic tar conversion and the prospective use of iron-based catalyst in the future development of biomass gasification: a review. Biomass Conv Bioref 2022;12(4):1369–92.